AGU PUBLICATIONS

Tectonics

RESEARCH ARTICLE
10.1002/2016TC004125

Key Points:
- Thermorheological variations and metamorphism are coupled in a crustal model
- Mineral assemblage variations and melt production strongly affect rheology of continental crust
- Metamorphic alterations induced by dyke intrusion can affect the tectonic evolution of continental crust

Correspondence to:
A. Lavecchia,
alessio@simula.no

Citation:
Lavecchia, A., S. R. Clark, F. Beekman, S. A. P. L. Cloetingh, and E. Burov (2016), Thermal perturbation, mineral assemblages, and rheology variations induced by dyke emplacement in the crust, *Tectonics*, *35*, 1137–1152, doi:10.1002/2016TC004125.

Received 20 JAN 2016
Accepted 26 APR 2016
Accepted article online 29 APR 2016
Published online 17 MAY 2016

Thermal perturbation, mineral assemblages, and rheology variations induced by dyke emplacement in the crust

Alessio Lavecchia[1,2], Stuart R. Clark[1], Fred Beekman[2], Sierd A. P. L. Cloetingh[2], and Evgueni Burov[3,4]

[1]Simula Research Laboratory, Fornebu, Norway, [2]Department of Earth Sciences, Utrecht University, Utrecht, Netherlands, [3]Institut des Sciences de la Terre Paris (ISTeP), University Pierre and Marie Curie, Paris, France, [4]Deceased 9 October 2015

Abstract We constructed a thermomechanical model to examine the changes in rheology caused by the periodic intrusion of basaltic dykes in a two-layered continental crust. Dyke intrusion can locally change the mineralogical composition of the crust in space and time as a result of temperature-induced metamorphism. In our models we paid particular attention to determine how different mineral assemblages and reaction kinetics during metamorphism impact on the thermomechanical behavior of the crust, in terms of differential stress values. We investigated several lithologies characteristic for intracontinental crust: (1) a quartz-feldspathic crust (QF), (2) a crust with a mineralogical assemblage resembling the average chemical composition occurring in literature (CC), and (3) a micaschist crust (MS). Our model shows that temperature profiles are weakly influenced by metamorphism, with negligible variations in the *T-t* paths. The results indicate that intrusion-induced changes in the crustal rheology are strongly dependent on mineralogical assemblage variation. The strength of a dyke aureole in the upper crust increases during dyke emplacement, which may cause migration of later dykes and influence the dyke spacing. In contrast, in the lower crust the strength of a dyke aureole decreases during dyke emplacement. Fast kinetics results in a ductile lower crust in proximity of the dykes, whereas slower kinetics leads to the formation of partial melts and subsequent switch from ductile to brittle behavior. Lithology exerts a dominant role on the quantity of melt produced, with higher volume percentages occurring in the MS case study. Produced melts may migrate and support acidic volcanic activity.

1. Introduction

Intraplate deformation is a result of a complex interaction between mantle and lithosphere processes, with feedback effects which are often difficult to foresee [e.g., *Burov et al.*, 2007, 2009]. This is of a particular relevance for continental rifting, where the interplay of plate boundary forces, plate-asthenosphere friction, and mantle upwelling determine the rifting evolution throughout its history [*Cloetingh et al.*, 2011]. It has been long acknowledged that the characteristics of the lithosphere (with particular emphasis to thermal structure and thickness) may exert a profound effect on the tectonic evolution of an area [e.g., *Sonder et al.*, 1987; *Braun and Beaumont*, 1989; *Dunbar and Sawyer*, 1989, *Buck*, 1991; *Bassi*, 1991]. Although extensional models including only mechanical stretching conditions have proven successful at describing many typical features of rifting areas [e.g., *McKenzie*, 1978; *Huismans et al.*, 2005], other common deformation characteristics occurring during extension can only be reproduced by taking into account more detailed lithospheric reconstructions.

It is well established that during initial rifting phases accommodation of deformation is mostly dominated by lithospheric stretching and characterized by the presence of large-scale border faults, whose presence defines a typical half-graben morphology [*Hayward and Ebinger*, 1996; *Ebinger et al.*, 1999]. A consensus is also growing on the important role of melt intrusion in favoring lithospheric breakup and extension. Analytical/numerical studies [e.g., *Buck*, 2004, 2006; *Bialas et al.*, 2010], supported by field evidences [e.g., *Björnnson et al.*, 1977; *Hjartardóttir et al.*, 2012; *Keir et al.*, 2006; *Wright et al.*, 2006, 2012] have demonstrated the intimate relationship between rifting episodes and melt emplacement, resulting in an extension accommodated by magma filling.

The presence of melts has been recognized in a variety of geodynamic settings [e.g., *Annen and Sparks*, 2002; *Annen et al.*, 2006; *Michaut and Jaupart*, 2006; *Solano et al.*, 2012] and facilitates the breakup of continental lithosphere. Its effect on the rheological characteristics of the intruded plate, however, is still poorly investigated. Many recent studies point out the importance of lithospheric rheological structure in lithosphere extension, especially in the analysis of dynamic topography and the interaction between plumes and plates in general [e.g., *Burov and Cloetingh*, 2009; *Cloetingh et al.*, 2013a, 2013b; *Burov and Gerya*, 2014]. However, the rheological

stratification currently adopted in many lithospheric models does not envisage the possibility that (1) the characteristics of the lithosphere are extremely variable both vertically and laterally, even at a very short scale, and (2) discontinuities along the lithosphere are not only inherited but also developed during the rifting processes.

The aforementioned heterogeneities may be of various nature, but among these, lithological variation may play a primary role in determining the rheological behavior of the lithosphere, both horizontally and vertically. In geodynamically active settings, rocks are subjected to important temperature-pressure variations. As a consequence, their mineralogical assemblage and fabric may change considerably. This is particularly true in the case of the crust, due to inherited chemical and mineralogical heterogeneity.

Furthermore, thermal perturbation is a direct cause of partial melting, especially when crustal/lithospheric thinning is accompanied by magmatic activity [e.g., *Annen and Sparks*, 2002; *Annen et al*., 2006; *Solano et al*., 2012]. The presence of magmas at crustal level is mainly due to asthenosphere decompression, partial crystallization of basaltic magmas and subsequent fractionation of more silica-rich melts, and/or partial melting of preexisting host rocks [e.g., *Annen et al*., 2006; *Solano et al*., 2012, and references therein]. A melt-intruded crust is a polyphase mush, characterized by considerably lower strength values [e.g., *Rosenberg and Handy*, 2005]. This, together with metamorphism, causes important deviations in the rheological behavior of rocks. Such deviations are focused most likely in the maximum deformation areas in the crust, where they may considerably influence the evolution of geodynamically active areas. This aspect, therefore, should be an integral part of future studies of crustal deformation in which intrusions and melts may occur.

In this paper we present the results of a 2-D thermomechanical model, designed to examine the changes in rheology of a continental crust which is subjected to a thermal perturbation representative of early magmatic phases of rifting. Our model takes into account different mineralogical assemblages and their variations with time, due to temperature-induced metamorphism. We adopted typical intracontinental lithologies, with a temperature- and melt-dependent rheology, and paid particular attention to determine how different mineral assemblage and metamorphism-related reaction kinetics may influence the mechanical behavior of the crust. The obtained results may contribute to reconstruct a more realistic response of the plates subjected to extension, especially in tectonic settings and/or rifting stages where the crust constitutes a significant percentage of the whole plate thickness.

Although the role of plumes as a direct cause of lithosphere extension and drifting has been the subject of intense debate [e.g., *Ziegler and Cloetingh*, 2004; *Natarov and Conrad*, 2012; *Burov and Gerya*, 2014], their role in triggering and focusing deformation has been acknowledged [e.g., *Rychert et al*., 2012]. Thus, a crustal rheology, coherent with petrological observations, may contribute to a better understanding of the interaction between "active" and "passive" rifting, with a particular attention to aspects related to the propagation of plume-related topography perturbations [*Burov and Cloetingh*, 2009].

2. Characteristics of the Crustal Model

2.1. Geometrical and Thermal Features

We used a 2-D thermal model that numerically simulates the temperature variations in a two-layered crustal section, induced by the growth of an intruded basaltic body over a time span of 2 Myr (Figure 1).

Our model comprises a 35 km thick crust with a lateral extension of 30 km, divided into two crustal layers with same thickness (17.5 km) but different density and mineralogical composition. The thermal loading is implemented by a cyclic series of "injected" dykes that build up a basaltic body with a thickness of 10 km. Each dyke has an individual thickness of 25 m and is added to the basaltic main body by outward lateral accretion to the left edge of the plate model.

The thermal evolution of the model is governed by the heat transfer equation (1):

$$\rho C_p \frac{\partial T}{\partial t} = k(T)\nabla^2 T + Q \tag{1}$$

where ρ is the density, C_P is the specific heat, T is the temperature, t is the time, k is the thermal conductivity, and Q is the internal heat production. The model does not take into account any advection of heat, because the dyke emplacement may be considered a quasi-instantaneous process, given a magma velocity in the order of meters per second [e.g., *Wilson*, 1981]. The numerical solution is obtained by using FEniCS [*Logg et al*., 2012], a collection of free scientific computing codes for finite element based on the automated solution of partial differential equations.

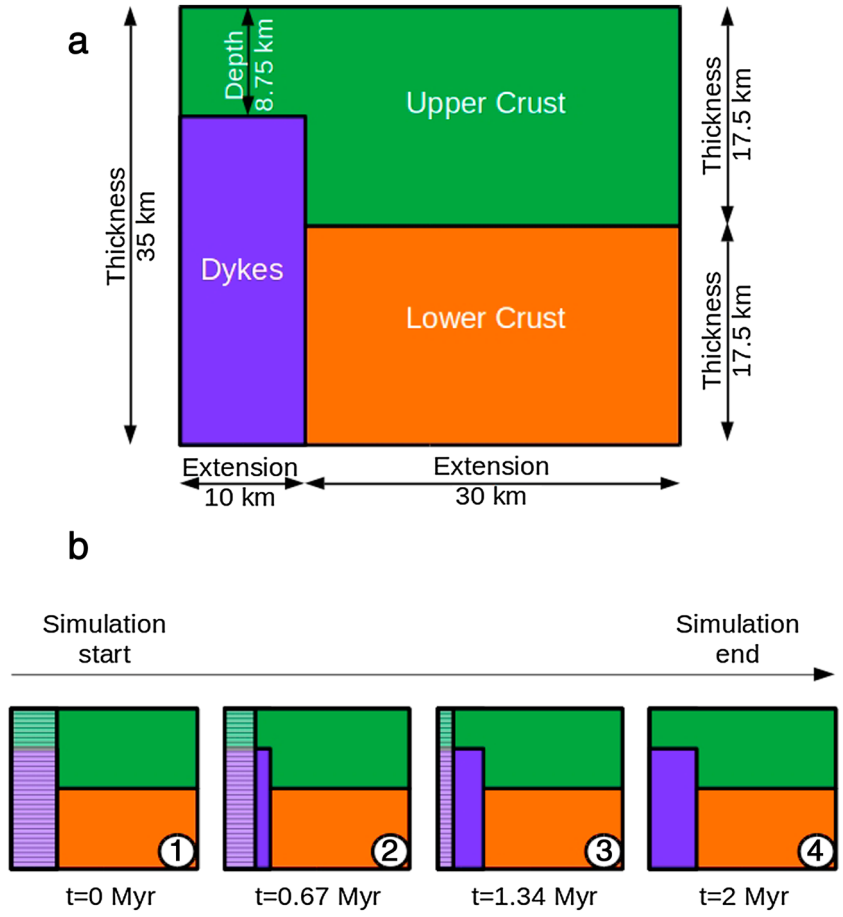

Figure 1. (a) Schematic representation of the 2-D model geometry. (b) Illustration for four different time steps (1–4) of the magma body growth. During each time step dykes are added to the main body by outward lateral accretion to the left edge of the model. Hatched left rectangle indicates the portion of the model not computed at different time steps.

The values assigned to the modeling parameters are given in Table 1. For the initial geotherm a fixed thermal conductivity (2.25 $W\,m^{-1}\,K^{-1}$), a surface temperature of 25°C, and a basal temperature of 750°C were used. These values were chosen in order to maintain the crust in thermal equilibrium with respect to the muscovite dehydration reaction and to avoid melt generation before the simulation starts. After dyke intrusion, the geotherm is updated by applying a temperature-dependent thermal conductivity, a fixed heat flux at the base of the crust of 27 $mW\,m^{-2}$, and a temperature-dependent heat flux calculated according to Newton's law of cooling (2) [see, e.g., *Incropera et al*., 2006]:

$$q_s = h(T - T_s) \tag{2}$$

where q_s is the heat flux, h is the convection heat transfer coefficient, T is the temperature at the surface, and T_s it the atmosphere temperature. The values adopted for q_s and h are chosen such that possible temperature fluctuations do not exceed ±6°C in the simulations.

The heat flux at the lateral boundaries has always been kept equal to 0, justified by the low thermal diffusivities that prevent fast heat transfer toward these edges.

The temperature-dependent thermal conductivity [*Clauser and Huenges*, 1995] varies according to the empirical equation by *Zoth and Hänel* [1988] (see Table 1). At $T \geq 200$–300°C the resulting values for conductivity are $\leq 2.0\,W\,m^{-1}°C^{-1}$, in agreement with experimental determinations [*Clauser*, 2009].

At the start of each model run, stability iterations are carried out to ensure equilibrium of the metamorphic associations assigned to the crustal layers, constant values of the thermal conductivity values, and small adjustments in the geotherm with the new boundary conditions.

Table 1. Thermal Parameters Adopted in the Model[a]

Parameter	Symbol and Equation	Value	References
Surface temperature (preliminary geotherm)	T_s	25°C	
Crust base temperature (preliminary geotherm)	T_b	750°C	
Magma emplacement temperature	T_m	1300°C	*Paterson et al.* [1998]
Magma crystallization temperature	T_c	1100°C	*Paterson et al.* [1998]
Density	ρ	Upper crust: 2650 kg m^{-3}	*Holbrook et al.* [1992]
		Lower crust: 2850 kg m^{-3}	*Holbrook et al.* [1992]
		Dykes: 2900 kg m^{-3}	*Carmichael* [1990]
Thermal conductivity	$A+\frac{B}{350+T(°C)}$	Upper and lower crust: $A=0.75$ W m^{-1}°C^{-1}; $B=705$ W m^{-1}	*Zoth and Hanel* [1988]
		Dykes: $A=1.18$ W m^{-1}°C^{-1}; $B=474$ W m^{-1}	
Surface heat flux	$q_s=h(T-T_s)$	$h=5$ W m^{-2} K^{-1}	*Incropera et al.* [2006]
Crust base heat flux	q_b	$2.7°10^{-2}$ W m^{-2}	
Lateral boundaries heat flux	q_l	0 W m^{-2}	
Specific heat	C_P	Upper crust: 1370 J kg^{-1} K^{-1}	*Bohrson and Spera* [2001]
		Lower crust: 1390 J kg^{-1} K^{-1}	*Bohrson and Spera* [2001]
		Dykes: 1480 J kg^{-1} K^{-1}	*Bohrson and Spera* [2001]; *Laube and Springer* [1998]
Latent heat of crystallization	LH	$4°10^5$ J kg^{-1}	*Spear* [1993]
Radiogenic heat generation	$A(z)=A_0e^{\frac{-z}{D}}$	$A_0=2°10^{-6}$ W m^{-3} $D=1.2°10^4$ m	*Gerya* [2010]

[a]When reference is not present, values have been chosen by the authors (see text for further explanation).

A novel aspect of our model is that the crustal heat production is not only due to radiogenic heat production but also to reaction enthalpy caused by intrusion-induced temperature variations and associated metamorphism. The radiogenic heat production rate has been conventionally assumed to be decreasing exponentially with depth [e.g., *Ranalli*, 1995]. This is a common approximation since heat generation rates of different rock types generally decrease with decreased silica content [e.g., *Vilà et al.*, 2010]. The depth-dependent radioactive decay law is as follows (3):

$$A(z)=A_0\exp\left(\frac{-z}{D}\right) \tag{3}$$

where $A(z)$ is the radiogenic heat production at depth z, A_0 is the radiogenic heat production at surface, and D is the characteristic depth. In our model, the adopted value of D represents an average of the different values reported in literature [e.g., *Lachenbruch*, 1968; *Jessop and Trevor*, 1978]. Values adopted are given in Table 1.

For the cooling of basaltic magma, the release of latent heat of crystallization has been taken into account by incorporating an effective specific heat instead of the true specific heat for the interval of crystallization between 1300 and 1100°C [*Paterson et al.*, 1998, and references therein]. The effective specific heat has been calculated on the basis of the formula by *Spear* [1993] (4):

$$C_{\text{eff}}=C_p+\frac{\text{LH}}{\Delta T} \tag{4}$$

where C_{eff} is the effective specific heat, C_P is the specific heat, LH is the latent heat of crystallization, and ΔT is the crystallization temperature interval. The values adopted in the simulation lead to an effective heat value of 2813 J kg^{-1} K^{-1} in the crystallization temperature interval (see Table 1).

2.2. Metamorphic Features

For a non quartz-feldspathic crust, any coherent model simulating the cooling of melts in the crust should take into account the possibility of metamorphic reactions due to the thermal perturbations. In our case, we have modeled prograde metamorphism in different mineralogical associations for the upper and lower crust (Table 2), adopting the following three combinations: (1) a crust composed of quartz (upper) and feldspars (lower) (model QF); (2) a crust with a mineralogical association resembling the chemical composition for

Table 2. Mineral Assemblages Adopted in the Model[a]

Crust Case Study	Upper Crust	Lower Crust
Quartz-feldspathic (QF)	qz100	pl100
Crust average chemical composition (CC)	chl13, ms13, qz37, pl23, kfs14	ms13, qz13, pl20, ky4, grt15, bt20, st2, kfs13
Micaschists (MS)	chl30, ms25, qz25, pl10, kfs10	ms10, qz20, pl15, ky5, grt10, bt25, st5, kfs10

[a]Values expressed as volume percentages.

upper and lower crust given by *Rudnick and Gao* [2003] (model CC); and (3) a sedimentary protolith, metamorphic crust (model MS).

For each of these three cases we analyzed both the initial and the postintrusion thermal evolution and the resulting variations in composition and rheology. More in detail, we have considered the most common mineral constituents in crustal rocks (quartz, plagioclase, K-feldspar, aluminosilicates, chlorite, muscovite, biotite, garnet, staurolite, and water), including the main metamorphic reactions leading to their appearance or consumption, and also the possibility to generate partial melting. Minerals belonging to aluminosilicates and chlorite, biotite, garnet, staurolite, and feldspars groups are treated as pure mechanical mixtures among end-members. The metamorphic grid is illustrated in (Figure 2).

The reaction stoichiometry has been calculated on the basis of oxides balance and kept fixed at different *T-P* conditions: (1) Ky-And-Sil, (2) 3Chl + Ms + 3Qz = Bt + 4Grt + 12Wt (3) 15Chl + 15Grt + 33Ms = 33Bt + 34Qz + 7St + 46Wt, (4) 4Bt + 7Qz + St = 5Grt + 4Ms + 2Wt, (5) Ms + 5Qz + 2St = 18Als + Bt + Grt + 4Wt, (6) 13Ab + 18Ms + 47Qz + 70Wt = 14Als + 4Kfs + L, and (7) 13Ab + 11Als + 13Bt + 47Qz + 31Wt = 9Grt + 4Kfs + L.

The temperature-pressure curves have been extrapolated by *Spear and Cheney* [1989], taking into account the results obtained by *Symmes and Ferry* [1992] and incorporating the effect of Mn in decreasing the temperature values needed for garnet stability. The muscovite and biotite dehydration reactions are calibrated on the basis of studies by *Vielzeuf and Holloway* [1988] and *Patiño Douce and Johnston* [1991] by assuming an approximated melt composition of 40qz, 30kfs, and 30pl, based on studies by *Luth et al.* [1964] and an oligoclase composition of plagioclase.

To account for eventual variations in the simulation thermal balance due to metamorphic reactions, their reaction enthalpy has been determined, according to the formula (5):

$$H = E + PV \tag{5}$$

where H is the enthalpy of the system, E is the internal energy, P is the pressure, and V is the volume. In our model we treat the influence of the enthalpy variations in the temperature equation as energy variations

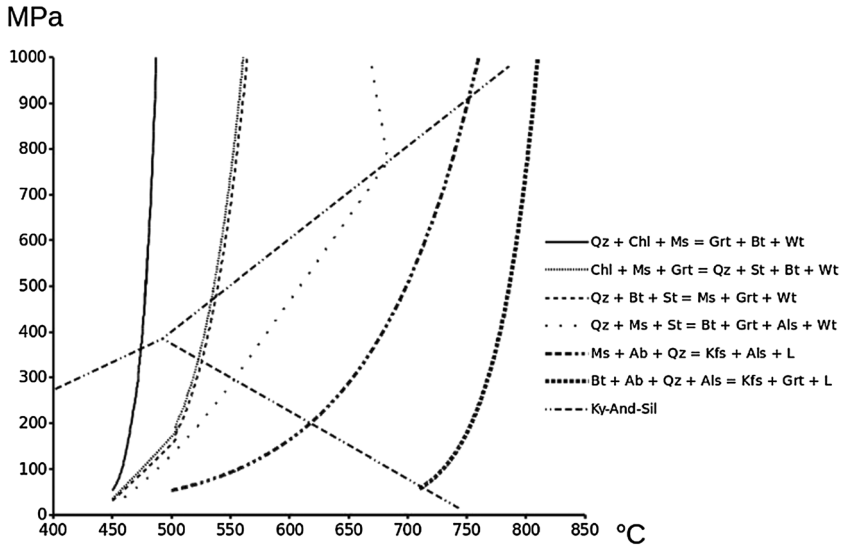

Figure 2. Reaction grid used to simulate metamorphism in the crust. Reactions in the legend occur with increasing temperature.

where appropriate temperature-pressure conditions are reached. This simplification has been adopted, since rock volume variations due to metamorphism seldom exceed 10%. Thus, as a first approximation, the *PV* term of the equation can be considered negligible in the enthalpy calculation.

For every mineral, we calculate the enthalpy of formation, according to *Philpotts and Ague* [2009] (6):

$$\Delta H = H_T^0 - H_{298}^0 = a(T - 298) + \frac{b}{2}\left(T^2 - 298^2\right) - c\left(T^{-1} - 298^{-1}\right) + 2d\left(T^{0.5} - 298^{0.5}\right) \quad (6)$$

where $H^0{}_T$ and H^0_{298} are the mineral enthalpy of formation at standard pressure and, respectively, given temperature and standard temperature, while a, b, c, and d are thermodynamic parameters, with values given by *Holland and Powell* [1998]. Afterward, we calculate the reaction enthalpy (7):

$$\Delta H_{\text{rreaction}} = \sum_{i=1}^{n} \Delta H_i - \sum_{j=1}^{m} \Delta H_j \quad (7)$$

where n and m are, respectively, the number of the products and the reactants in the metamorphic reaction. The muscovite- and biotite-dehydration melts are similarly treated, by transforming their latent heat of fusion ($4 \cdot 10^5\,\text{J kg}^{-1}$) [*Spear*, 1993] in formation enthalpy.

The metamorphism in our model is not instantaneous but develops over a certain time span, ruled by imposed values of reaction kinetics and in response to cyclic dyke intrusion. To implement a realistic reaction kinetics scenario, we took garnet growth velocities as estimated by *Cashman and Ferry* [1988] and *Christensen et al.* [1989, 1994] and related these to garnet population density and crystal dimensions estimated by *Cashman and Ferry* [1988], *Pattison and Tinkham* [2009] and *Gaidies et al.* [2011]. Garnet growth characteristics are among the best studied and therefore adopted for our simulations. By crossing data, we obtained values for garnet growth velocities ranging from $50\,\text{mol m}^{-3}\,\text{yr}^{-1}$ to $500\,\text{mol m}^{-3}\,\text{yr}^{-1}$ and even up to $5000\,\text{mol m}^{-3}\,\text{yr}^{-1}$. These values have been used to calibrate the other minerals' growth velocities, depending on their stoichiometric index in the studied reactions. Where garnet was not involved, the reaction kinetics of the other minerals has been determined by the weighted mean of values in the garnet-occurring reactions kinetics.

2.3. Rheological Features

Two-dimensional strength profiles have been obtained using the frictional criterion for the brittle field and the power law creep equation for the ductile field. For every deformation mechanism the differential stress σ (i.e., $\sigma = \sigma_1 - \sigma_3$) has been calculated. We assumed as dominant deformation the mechanism that requires the least differential stress.

For the frictional criterion we have used the equation (8) [*Sibson*, 1974]:

$$\sigma_b = \sigma_1 - \sigma_3 = \beta\,\rho g z(1 - \lambda) \quad (8)$$

where $\sigma_b = \sigma_1 - \sigma_3$ is the friction-related differential stress (compression is positive). β is a dimensionless parameter depending on the frictional coefficient and deformational regime, ρ is the rock density at depth z, and g is gravity acceleration. The pore fluid factor λ (ratio of pore fluid pressure to lithostatic pressure) is set to 0.4, which is representative for hydrostatic pore fluid pressures. For an extensional tectonic regime and a uniform friction coefficient $\mu = 0.75$ for all rocks, $\beta = 0.75$ for our crustal model [*Ranalli*, 1995]. The values of density adopted in the model are given in Table 1.

The creep flow law implemented in the model is [e.g., *Gerya*, 2010; *Karato*, 2008; *Ranalli*, 1995]

$$\dot{\epsilon} = Ah^m(\sigma_d)^n \exp\left(\frac{-E + V_a P}{RT}\right) \quad (9)$$

where $\dot{\epsilon}$ is strain rate, h is the grain size raised to the power of the parameter m, σ_d is the differential stress (similarly to σ_b), P is the pressure, R is the gas constant, T is the temperature, and A, n, E, and V_a are the mineral's rheological parameters. Ductile deformation in the crust mainly occurs by dislocation creep [e.g., *Kirby*, 1985], for which $m = 0$ and V_aP is negligible (since $V_aP \ll E$).

The rheological parameters adopted in the model for each mineral are listed in Table 3. The parameters adopted for staurolite and aluminosilicates are a mean between "weak" minerals (quartz and feldspars) and "strong" minerals (garnet) [*Kruhl and Vernon*, 2005; *Kruhl et al.*, 2007]. The rheological parameters for the single minerals were used to calculate the parameters of the multiphase rock for each time step, following the average procedure suggested by *Ji and Zhao* [1993] and *Ji et al.* [2003].

Table 3. Rheological Parameters for Minerals in the Model

Model Mineral	Adopted Mineral	A ($MPa^{-n} s^{-1}$)	n	E ($kJ\,mol^{-1}$)	References
Chlorite	Mica	1.10E−15	18	51	*Kronenberg et al.* [1990]
Muscovite	Mica	1.10E−15	18	51	*Kronenberg et al.* [1990]
Biotite	Mica	1.10E−15	18	51	*Kronenberg et al.* [1990]
Quartz (dry)	Quartz	1.10E−04	4	223	*Gleason and Tullis* [1995]
Plagioclase	Albite	2.34E−06	3.9	234	*Shelton and Tullis* [1981]
K-feldspar	Albite	2.34E−06	3.9	234	*Shelton and Tullis* [1981]
aluminosilicates		2.34E+01	4	410	Chosen by authors; see section 2.3
Staurolite		2.34E+01	4	410	Chosen by authors; see section 2.3
Garnet	Pyralspite	2.76E+02	3	444	*Wang and Ji* [1999]

The implementation of partial melting, due to muscovite- and biotite-dehydration reactions, requires a separate approach for partially molten rocks. In our simulation we have identified two rheological thresholds when melting is occurring. A first rheological threshold occurs with melt fraction $\Phi = 6$–8%, corresponding to the melt connectivity transition (MCT) [*Rosenberg and Handy*, 2005]. In this melt fraction interval, the brittle strength of the rock diminishes, according to the relationship (10):

$$\log_{10}(\sigma_{\mathrm{bMCT}}) = \log_{10}(\sigma_b) - 0.5\left\{1 - \cos\left[\pi\left(\frac{\phi}{2} - 3\right)\right]\right\} \tag{10}$$

where Φ is the melt fraction, σ_{bMCT} is the brittle strength when $\Phi = 6$–8%, and σ_{b} is the brittle strength of the melt-free rock. The decrease in the crustal brittle strength between the indicated melt percentages is 1 order of magnitude for $\Phi \geq 8\%$.

The second rheological threshold is reached when $\Phi = 30$–40% and corresponds to the solid to liquid transition (SLT) [*Rosenberg and Handy*, 2005], equivalent to the rheologically critical melt percentage [*Arzi*, 1978]. For these melt fraction values the strength of the whole rock resembles the strength of a melt-crystal mush with features in between two extreme terms: a rock with a rheology influenced by the presence of melt batches and a melt with a viscosity affected by the presence of crystals. Thus, in calculating the mush strength, we take into account (1) the viscosity (and consequently, the strength) of a pure, crystal-free melt and its variations with temperature; (2) The viscosity variation of the produced melt, as a function of different crystals percentage; and (3) The mush strength when a melt percentages is $\Phi = 30$–40%.

The viscosity of the crystal-free melts has been calculated by using the Arrhenius equation (11) [*Dingwell*, 1995]:

$$\log_{10}(\eta_T) = \log_{10}(\eta_0) + 2.303\frac{E}{RT} \tag{11}$$

where η_T is the melt viscosity at temperature T, η_0 is a preexponential factor, E is the activation energy, and R is the gas constant. In order to calibrate the viscosity curve, data have been excerpted from *Shaw* [1965] for magmas with 4 vol % H_2O, leading to values $\eta_0 = -3.0$ and $E = 36{,}500$. The obtained values for crystal-free melts have been inserted in the Einstein-Roscoe equation (12) [*Roscoe*, 1952], to calculate the crystal-melt system viscosity:

$$\eta(\phi, T) = \eta_T\left(1 - \frac{\phi}{\phi_c}\right)^{-2.5} \tag{12}$$

where $\eta(\Phi)$ is the mush viscosity at a certain melt fraction Φ and temperature T, and Φ_c is the critical melt fraction when the crystals-melt system assumes features of a solid. Subsequently, the magma strength has been calculated by characterizing the system as a Newtonian fluid (13):

$$\sigma_M = \eta(\phi, T)\dot{\epsilon} \tag{13}$$

where σ_{M} is the mush strength. The simulation takes into account the transition rock strength/mush strength, in a similar manner to the MCT transition, according to the relationships (14) and (15):

$$W_{\mathrm{M}} = 0.5\left\{1 + \cos\left[\pi\left(\frac{\phi}{10} - 3\right)\right]\right\} \tag{14}$$

$$\sigma = \sigma_{\mathrm{R}} W_{\mathrm{M}} + \sigma_{\mathrm{M}}(1 - W_{\mathrm{M}}) \tag{15}$$

where W_{M} is a weight factor, dependent on the melt fraction (taking the value 1 when $\Phi = 30$ vol % and 0 when $\Phi = 40$ vol %) and σ_{R} is the solid rock strength.

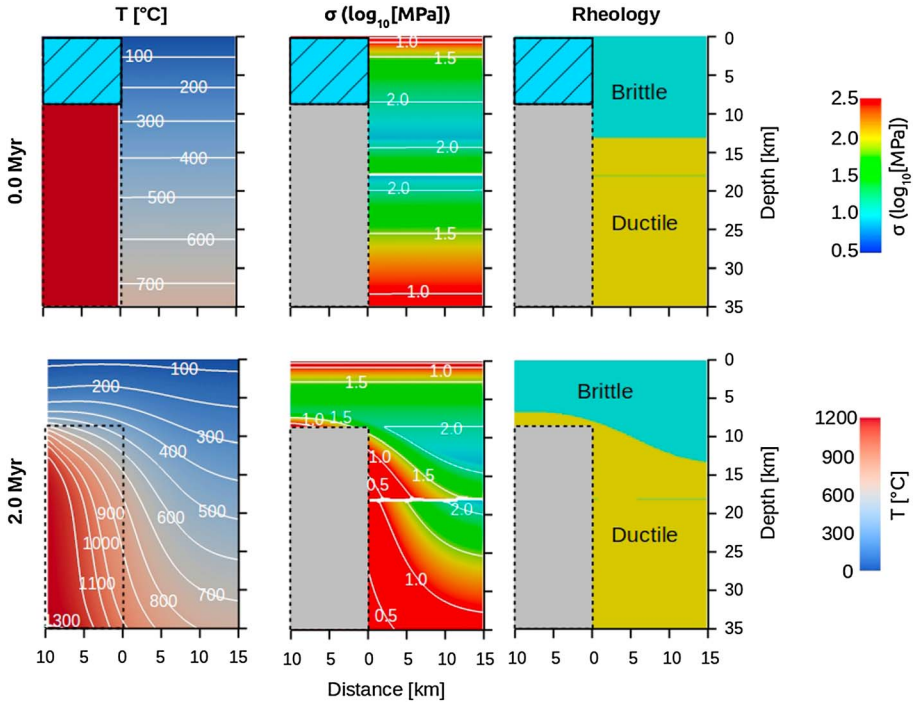

Figure 3. (left column) Temperature, (middle column) differential stress, and (right column) brittle-ductile transition contour sections for a quartz-feldspathic (QF) crustal composition, at initial and final simulation time steps. (top row) The initial crustal configuration. (bottom row) The crustal configuration at the end of simulation. Temperatures are expressed in °C, while differential stress values are expressed as log10 of the value in megapascals. Dimensional values are expressed in kilometers. The light blue field in the brittle-ductile transition contour sections represents the brittle behavior, while the yellow field represents the ductile behavior. The blue hatched squares at the top of the dyke body represent the portion of the crust which is initially not included in the computation. The orange rectangles indicate the model portions simulating the dykes, not included in the strength and rheological calculations.

3. Modeling Results and Sensitivity

3.1. Modeling Results

Our modeling results are presented as contoured sections for selected time steps (Figures 3, 5, and 7). A more detailed view in the dyke aureole is presented as temperature-time paths (Figure 4) in three selected points located at a distance of 250 m from the first intruded dyke and at depths of 10, 20, and 30 km. Moreover, Figure 6 shows a stress-time projection of a *Y* transect, located in the crust at a distance of 250 m from the dyke-crust boundary.

The temperature contours (Figure 3) show that thermal perturbation related to dyke intrusion persists after 2 Myr, and it is still intense after the emplacement of the last dyke. The periodical emplacement of dykes produces a quick but smooth temperature increase with time, followed by a slow, constant decrease. The smoothness of the temperature profile is due to the progressive emplacement of thin dykes equally distributed during simulation time and is in agreement with results obtained by *Annen and Sparks* [2002].

In a crust with quartz-feldspathic composition (QF case study), the *T-t* path relative to the upper crust (Figure 4) shows a temperature increase up to a temperature peak of approximately 495°C, reached after 400 kyr of simulated time. In the lower crust, at a depth of 20 km, the temperature peak is 820°C reached after 1.57 Myr, while the peak temperature has not been reached in the lower crust at a depth of 30 km, and the maximum registered temperature is 935°C.

The *T-t* path geometry predicted for polymineralic mineralogical assemblages (Figure 4) resembles the trend of a quartz-feldspathic crust, albeit with slightly lower temperatures. These differences, which are described in more detail later on, are maximum between the *T-t* paths relative to a quartz-feldspathic and a micaschists mineral assemblage and for slow reaction kinetics. Temperature variations are negligible in the lower crust

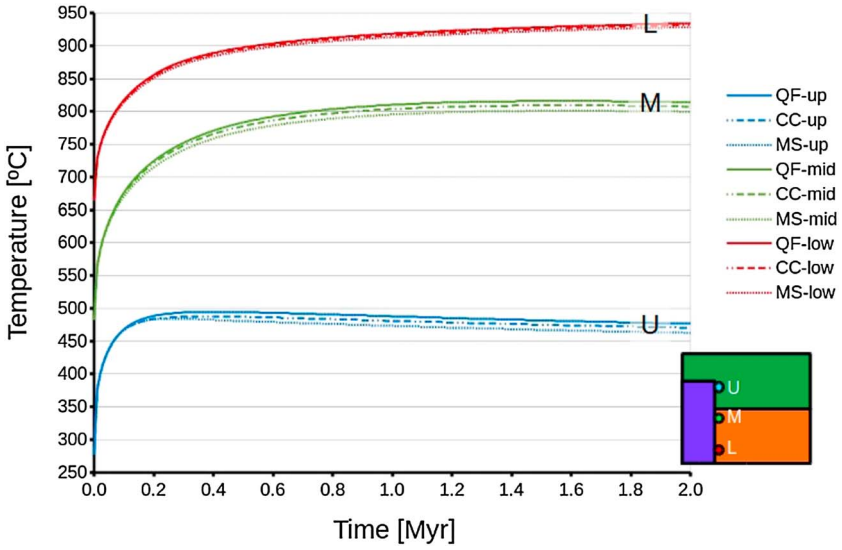

Figure 4. *T-t* paths in different locations within the dyke aureole. Paths are for slow kinetics. Circles indicate locations of points selected for *T-t* plots (see transect); every point is located at 250 m away from the dykes-crust boundary at depths of, respectively, 10 km (U), 20 km (M), and 30 km (L).

at depths greater than 30 km but tend to increase at shallower depths, with lower peak temperature and subsequent slightly faster cooling. Temperature differences become negligible at greater distances from the dykes-crust boundary.

The different mineralogical assemblages adopted during the simulations determine strong variations in the crust differential stress (σ) values and its rheological behavior (Figure 5). In the QF model, the chosen geotherm determines a crustal rheological transition at an approximated depth of 13 km, corresponding to a temperature of 350°C. Brittle behavior is restricted to a thin layer located in the uppermost lower crust and corresponding to a temperature of 450°C. The thermal perturbation due to melt emplacement results in a notable uprise of the brittle-ductile transition and in a strong decrease in crustal strength.

If a mineralogical assemblage approximating an average crust chemical composition (CC model) is adopted (Figure 5), the upper crust is characterized by a marked decrease in differential strength values and a shallowing of the brittle-ductile transition (depth around 8 km, *T* around 260°C). In contrast, the lower crust shows higher differential strength values (approximately 320 MPa) and is partially brittle (depth of rheological transition around 24 km, *T* around 570°C). The low σ values in the upper crust are due to a high mica content, whereas in the lower crust the different composition and metamorphism determine an enrichment in minerals characterized by high strength values (mostly garnet) and with a subsequent deepening of the brittle-ductile transition. Subsequent to dyke intrusion, the thermal perturbation causes an overall decrease in strength, except in a thin lateral aureole in the upper crust and at the top of the dyke body, where we predict an abrupt increase (and later decrease) in σ values. This σ trend is due to the enrichment in strong minerals (mostly garnet) at the expenses of micas (mostly chlorite) in the first stages of simulation, followed by a further temperature increase and subsequent decrease in σ values. This increase-decrease in rock strength is accompanied by a transition from brittle to ductile behavior of the aureole, evidencing the alternation between metamorphic and thermal control on rock rheology.

After 800 kyr the innermost part of the upper aureole is characterized by brittle behavior, albeit with low strength values. This low-strength nucleus is the result of the generation of melts (up to a quantity of 8 vol %) and capable to break up the rock's solid framework (i.e., the structure, constituted by crystals, representing the rock's continuous phase and determining its rheological characteristics). When compared to fast kinetics, a slow reaction kinetics results in a smoother transition in the upper crust from weak rocks to a strong aureole; also, the melt nucleus is slightly more extended. Furthermore, partial melting also occurs in the lower crust, up to a distance of 10 km, but melting percentages do not exceed 5 vol %. The SLT threshold is thus not reached, and the lower crust still keeps a solid framework.

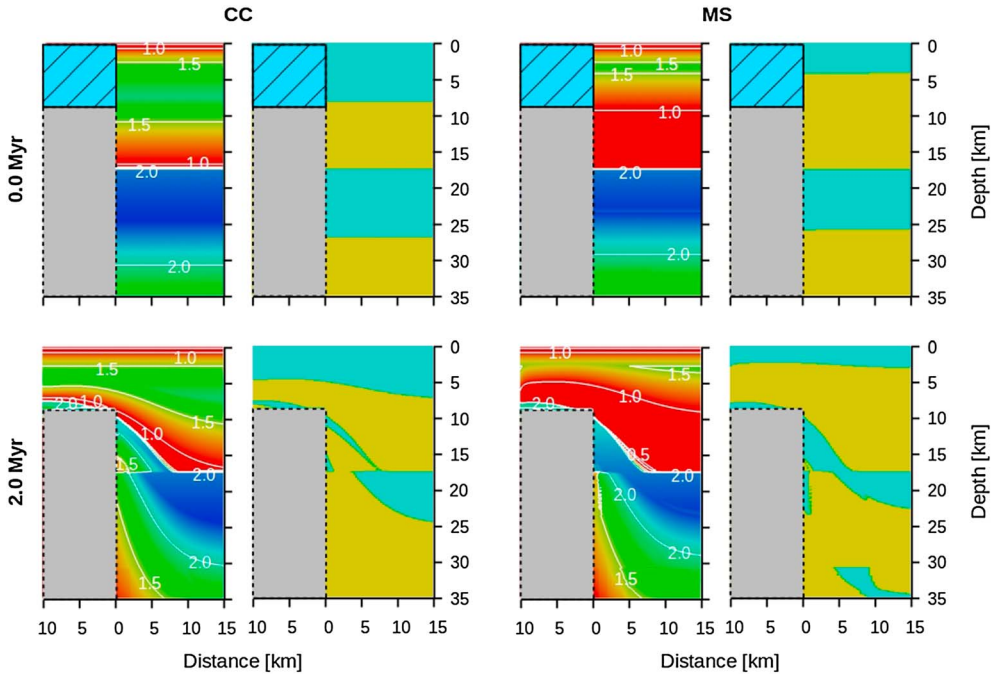

Figure 5. Differential and brittle-ductile transition contour sections for a mineralogical assemblage approximating average crustal composition (CC) and micaschist crust (MS), taking into account a slow reaction kinetics. For color scale, see Figure 3. (top row) The initial crustal configuration. (bottom row) The crustal configuration at the end of simulation. (first and second columns) Relative to CC case study. (third and fourth columns) Relative to MS case study. Temperatures are expressed in °C, while differential stress values are expressed as log10 of the value in megapascals. Dimensional values are expressed in kilometers. The light blue field in the brittle-ductile transition contour sections represents the brittle behavior, while the yellow field represents the ductile behavior. The blue hatched squares at the top of the dyke body represent the portion of the crust which is initially not included in the computation. The orange rectangles indicate the model portions simulating the dykes, not included in the strength and rheological calculations.

In the micaschist crust (MS) model, where a micaschists mineralogical assemblage is implemented, the chosen geotherm determines a very weak upper crust with a brittle-ductile transition less than 4 km deep, at a temperature of 130°C (Figure 5). Compared to the CC model, the lower crust is also weaker, with a brittle-ductile transition depth of 22 km (T 530°C), but not as weak as in the QF model.

Dyke-induced thermal metamorphism in the upper crust determines strong mineralogical associations, resulting in a consistent brittle domain in the upper lateral aureole. The lower crust also is deeply affected by reaction kinetics variations: when a slow kinetics is adopted, the melt percentage may reach values $>$15%, with subsequent breakup of the rock solid framework. Consequently, contoured sections in Figure 5 show a brittle interval at the base of the lower crust, appearing immediately after the emplacement of the first dykes (i.e., the first represented time steps). This brittle interval slowly migrates toward more peripheral parts of the base of the crust, suggesting that crustal deformation is controlled initially by melt. The metamorphism also affects the top of the lower crust, where a 1 km thick brittle domain develops at the dykes-host rocks boundary.

Variations in crustal differential stress values are largest in the proximity of the intruding dykes (Figure 6). In the QF model, the σ trend is in general agreement with temperature variations, which is not the case for the CC and MS models. When a polymineralic crust is taken into account, we observe in the first 200 kyr a sharp increase in differential stress values, caused by dyke-induced metamorphism. This is particularly evident in the upper crust of the MS model. In the CC model the strength increase is followed by a rapid decrease due to the subsequent thermal perturbation and generation of melts during the last time steps. In the MS model, the top of the lower crust is characterized by a brittle interval (related to the presence of partially molten rocks close to the intrusion-crust boundary), which, however, is too thin to be detectable in the stress contour sections.

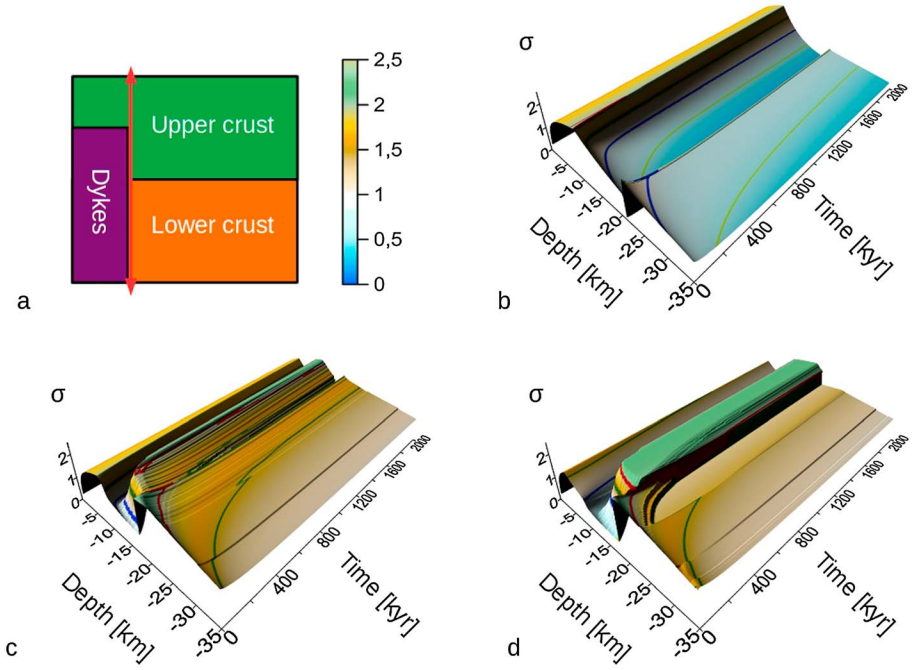

Figure 6. Differential stress-time projections along a transect located in the crust, at a distance of 250 m from the dykes-crust boundary; (a) location of the measurement profile and color scale, and σ-t trend in the (b) QF, (c) CC, and (d) MS case studies. σ is expressed as log10 of the value in megapascals. The isolines in Figures 6b–6d indicate the reference values of 1.0 (blue), 1.5 (green), and 2.0 (red).

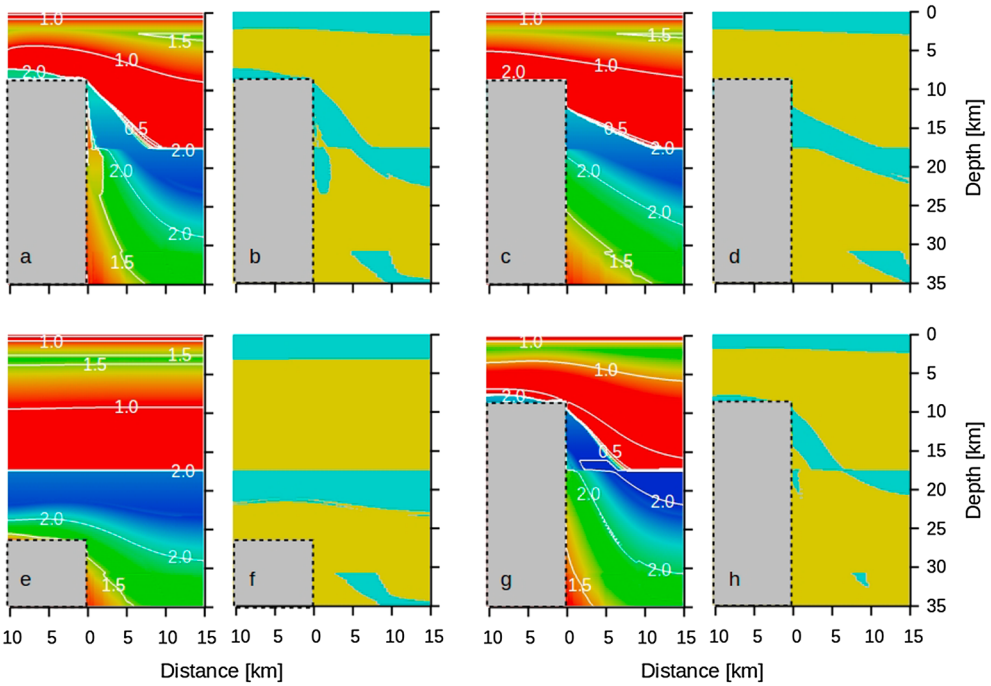

Figure 7. (a, c, e, g) Differential and (b, d, f, h) brittle-ductile transition contour sections for a micaschist crust (MS), when different parameters are tested. All panels refer to the end of simulation. Ten dykes with thickness of 1 km, intruded in a time span of 2 Myr (Figures 7a and 7b); a 10 km dyke body intruded in a time span of 10 Myr (Figures 7c and 7d); dyke body top at a depth of 26,250 m (Figures 7e and 7f); λ value = 0 (Figures 7g and 7h). For color scale see Figure 3.

3.2. Parameter Sensitivity

We have tested the sensitivity of our models by varying several parameters of the MS model with low reaction kinetics, as this model proved to be the most sensitive to metamorphism and melt generation (Figure 7).

First, to assess if the intrusion rate exerts a major control on the rheology, we tested our model (1) by considering a set of 10 dykes, each with a thickness of 1 km, intruding the crust over a period of 2 Myr, thus simulating instantaneous injections of huge quantities of melts followed by long periods of zero melt emplacement and (2) by expanding the overall intrusion time to 10 Myr, assuming a constant growth of the dyke body, with a resultant melt intrusion rate of 1 mm/yr.

Results show that when dyke thickness increases while the growth time of the whole magmatic segment remains constant, the geometry of the brittle-ductile transitions does not show major variations. Metamorphic aureoles are somewhat larger, and the basal brittle interval caused by partial melting shifts toward more peripheral parts of the model. These differences do not exceed a few hundreds of meters and therefore can be neglected, except for the top of the lower crust where the brittle domain reaches an average thickness of 3 km. Moreover, the tests show that variations in melt production also are negligible and that final differential stress values are reduced, with minimum values at the base of the upper crust.

Rheological variations become more pronounced when we adopt a longer simulation time for the growth of the intrusive magma body, allowing the thermal perturbation to reach more peripheral parts of the crust. This observation is in line with results by *Daniels et al*. [2014]. An opposite effect of the slower intrusion rate is the reduction in temperature peaks, especially in the upper crust. The combined effect results in a larger upper metamorphic aureole but does not affect the uppermost intruded rocks.

Although partial melting at the base of the crust affects brittle behavior of the rocks at a farther distance from the dykes-crust boundary, it shows no substantial first-order variations. This confirms the thermal control already observed in the dyke lower aureole in the previous simulations. Differences in differential stress values follow the earlier observed trend in the brittle-ductile transition, with higher values in the proximity of the intruded dykes.

Other tests involved the intrusion depth, with default values of 17.5 km (corresponding to the upper-lower crust boundary) and 26.25 km (half thickness of the lower crust). The temperatures computed in the tests are considerably less than those of the previous runs, and variations in differential stress values and rheology are consequently also smaller. An exception occurs at the top of the dyke body where temperatures reach 800°C for an emplacement depth of 26.25 km. However, as the reduced volume of emplaced magmas does not allow melt percentages higher than 4 vol %, the solid crust framework is maintained and no brittle intervals develop in the thermally perturbed lower crust.

The final test involves setting $\lambda = 0$, which results in an uplift of the brittle-ductile transition by 1 km in the upper crust and by 2 km in the lower crust. Moreover, the intracrustal brittle domains located at the contact with the dyke body are considerably reduced in size, and the crustal strength increases, with maximum σ values of 420 MPa.

4. Discussion

The results of our simulations show that different lithologies may exert a first-order control on both the strength and the rheological behavior of the crust. Another outcome is that the fertility of the crust (i.e., its capacity to generate melts at a given temperature) cannot be established a priori by assuming a direct correlation between anatexis and reached temperature peaks. In contrast, the composition of the crust exerts a primary role and must be taken into account.

The pristine QF case study (Figure 3) demonstrates the dominant control of temperature on the rheology of the crust. Here we observe that the isodifferential stress contour lines follow the isotherms, with the only exception at the upper-lower crust boundary. This observation is supported also by the geometry of the brittle-ductile transition, which lies at a temperature between 350°C and 390°C (assuming $\lambda = 0.4$). The thermal perturbation propagating from the intruding magma body causes a pronounced decrease in crustal strength, in agreement with the findings by, e.g., *Buck* [2004; 2006]. When more complex lithologies are considered, the crustal rheology exhibits a pronounced dependence on mineral assemblages, which therefore may result in important deviations in tectonic deformation of a crust subjected to heating and extension.

Heat absorption by metamorphism and melt generation reduces the thermal perturbation in our model (Figure 4), although temperature differences are negligible at a first order of approximation. At the same time, metamorphism and melt generation do exert a main control on the rheological features of the crust, especially within a distance of a few kilometers from the dykes-crust boundary (Figure 5). Differently from previous studies [e.g., *Buck*, 2004, 2006; *Daniels et al*., 2014], the thermal perturbation in the upper crust causes an increase in the rock strength and a change in the rheology of the host rocks. Furthermore, the depth of the brittle-ductile transition in the lower crust significantly increases to 23 to 25 km, roughly corresponding with the 600°C isotherm. This result is in agreement with findings by *Daniels et al*. [2014].

The extension of the aureole 2 Myr after intrusion is much smaller when the intrusion rates are 1 mm/yr, compared to a fast value of 5 mm/yr (Figure 7). In addition, the brittle aureole developed in 10 Myr is more extended than the one developed in 2 Myr. It, however, does not develop in proximity to the uppermost part of the magma body (Figure 7), which is consistent with the temperatures controlled by the intrusion rates. Thus, the geometry and extension of a brittle aureole depend on the adopted intrusion rates: low intrusion rates will lead to laterally more extended and vertically less extended metamorphic aureoles.

Another important parameter appears to be the reaction kinetics: we predict in both the CC and MS case studies a less extended brittle aureole for faster kinetics. This is not due to temperature but to a more effective mica consumption, resulting in relatively higher volume of strong minerals (such as garnet). The strong aureole located at the base of the upper crust may hamper magma ascent in proximity of older dykes and instead promote the emplacement of sills along the upper-lower crust boundary (already favored by the density jump). Consequently, in a sedimentary host rock setting, this may constitute an alternative explanation to other dyke spacing mechanisms [e.g., *Bunger et al*., 2013; *Maccaferri et al*., 2014].

An increase in rock strength may also occur in the lower crust and may be coupled with an extended partial melting at its base. Here melt production does not exceed the Rheological Critical Melt Percentage (RCMP) due to both reduced temperatures and crust fertility, in agreement with *Solano et al*. [2012]. The quantity of melts retained by the crust in partially molten intervals is uncertain, depending intrinsically on the quantity of melt and its viscosity. Melt migration is generally hampered by the high viscosity of the fluid [*Laporte and Watsons*, 1995]. However, results by *Brown* [2007, 2010a, 2010b, 2013] show that when a differential stress is applied melt can segregate at fluid fractions ≤ 7 vol %, leaving approximately 1 vol % melt, retained on grain boundaries [*Holness and Sawyer*, 2008; *Marchildon and Brown*, 2002; *Sawyer*, 2001]. According to our results, the presence of migmatites is mainly foreseen at the base of the crust and for depths larger than 30 km, producing a migmatitic layer of approximately 5 km thickness. This is in agreement with migmatitic paragneisses exposed in other deep crustal intervals, e.g., in Calabria [*Caggianelli and Prosser*, 2001, 2002; *Del Moro et al*., 2000]. Furthermore, these are also the most favorable layers where crustal melt migration may occur. If conditions for melt movement are reached, generated melts may reach shallower levels, generating and/or contributing to a coeval acidic volcanism, as observed in rift areas, such as the Afar Rift and surroundings [e.g., *Mohr*, 1991, and references therein; *Wolfenden et al*., 2004; *Ayalew and Gibson*, 2009; *Bastow et al*., 2011; *Natali et al*., 2011]. However, our model shows that a slow reaction kinetics favors anatexis and determines a higher melt production, since micas are not only reactants for melt production but also for other reactions occurring at lower temperatures not involving melt generation.

When a different thickness of the intruded dykes is adopted (Figure 7), while keeping the intrusion rate constant, we do not observe marked variations in the crust fertility, which is in agreement with results by *Annen and Sparks* [2002] and *Annen et al*. [2006]. Variations in produced melt volumes are also negligible, even for higher intrusion rates. This is in contrast with findings by the aforementioned authors but can be explained by the fact that in our simulations melt production is foreseen if minerals are still available and not consumed by previous metamorphic reactions. Thus, our results show that when temperatures are appropriate for melting, lithology exerts a primary control on crustal fertility.

In such cases, where lithology indeed exerts a main control on the quantity of melt generated in the crust, temperatures and thermal diffusivity also influence the volume of rocks affected by anatexis. At the end of a model run, melt is generated up to a distance of 20 km from the dykes-crust boundary. However, in our simulations the intruded body maintains a temperature higher than the established crystallization temperature (1100°C) in a substantial part of its volume. In addition, the *T-t* paths in the aureole, relative to a point located at a depth of 30 km, show that the temperature is constantly increasing up to the end of the model

simulation. This suggests that the crust might be subjected to further heating over a longer time span, especially in the lower crust, and that therefore a larger part of the crust may be affected by anatexis. As a result, the base of the crust can be marked by a migmatite layer, where the relative weakness and the preexisting melt veins [*Rosenberg and Handy*, 2005] may favor the magma ascent from underplated bodies.

5. Conclusion

We have investigated the thermorheological behavior of a two-layered, polymineralic crust affected by a thermal perturbation caused by lateral intrusion of melts during extension phases. The obtained model predictions were compared with results of a simpler two-layered monomineralic crust.

During an intrusion-induced temperature increase, a quartz-feldspathic crust shows a significant decrease in strength values, coherently with the temperature propagation in time. The crustal response becomes even more complex when metamorphism is taken into account. In the investigated models the lithology variations exert a main control as metamorphism may cause a transition from ductile to brittle behavior in the crust for increasing temperatures. These model predictions differ from results from previous studies [e.g., *Buck*, 2004; 2006]. This is particularly evident in the upper crust, where the presence of a wedge-shaped brittle body is predicted in all our simulations.

Another main factor controlling the rheology of the crust is the presence of melts. We have tested during our simulations that the amount of melt produced is sufficient to exceed the MCT and to cause breakup of the solid framework of rocks. Melts, therefore, promote brittle behavior in the crust and a reduction of strength values.

Differently from previous studies [e.g., *Annen and Sparks*, 2002; *Annen et al*., 2006], we observe that the crust fertility is mainly influenced by (1) lithology and (2) reaction kinetics. For fast reaction kinetics, the obtained melt fraction was considerably less, whereas slow reaction kinetics enhances the melt productivity by preservation of reactants for muscovite and biotite dehydration melting. This, therefore, plays a key role in changing the rheological behavior of the lower crust, with, for instance, brittle behavior in the case of a slow kinetics and ductile behavior when fast kinetics is adopted. The importance of lithology and reaction kinetics over temperature for melt production is also tested when melt intrusion rate variations are introduced: in all tested cases, obtained melt fractions show no significant differences.

The more complex rheological stratification resulting from dyke intrusion might lead to important deviations from expected rheological behavior of the crust during extension. This, for instance, could contribute to an explanation for the observed spacing of dykes during melt intrusion in extensional settings. Our findings suggest that the distance between dykes may be influenced by the increase in strength caused by previous melt intrusions.

Acknowledgments

This study has been funded by Simula Research Laboratory, Norway. We thank A. Caggianelli and G. Ranalli for detailed, constructive comments. L. Vynnytska provided useful remarks on the numerical part of the work. C. Spiers is also thanked for comments on the final stages and future perspective of the project. An anonymous reviewer, the Chief Editor, and the Associate Editor are also thanked for the constructive criticism. Data for this paper are available by contacting the corresponding author.

References

Annen, C., and R. S. J. Sparks (2002), Effects of repetitive emplacement of basaltic intrusions on thermal evolution and melt generation in the crust, *Earth Planet. Sci. Lett.*, *203*, 937–955.

Annen, C., J. D. Blundy, and R. S. J. Sparks (2006), The genesis of intermediate and silicic magmas in deep crustal hot zones, *J. Petrol.*, *47*, 505–539, doi:10.1093/petrology/egi084.

Arzi, A. (1978), Critical phenomena in the rheology of partially melted rocks, *Tectonophysics*, *44*, 173–184.

Ayalew, D., and S. A. Gibson (2009), Head-to-tail transition of the Afar mantle plume: Geochemical evidence from a Miocene bimodal basalt–rhyolite succession in the Ethiopian Large Igneous Province, *Lithos*, *112*, 461–476.

Bassi, G. (1991), Factors controlling the style of continental rifting; insights from numerical modelling, *Earth Planet. Sci. Lett.*, *105*, 430–452.

Bastow, I. D., D. Keir, and E. Daly (2011), The Ethiopia Afar Geoscientific Lithospheric Experiment (EAGLE): Probing the transition from continental rifting to incipient seafloor spreading, in *Volcanism and Evolution of the African Lithosphere*, edited by L. Beccaluva, G. Bianchini, and M. Wilson, *Geol. Soc. Am. Spec. Pap.*, *478*, 51–76.

Bialas, R. W., W. R. Buck, and R. Qin (2010), How much magma is required to rift a continent?, *Earth Planet. Sci. Lett.*, *292*, 68–78.

Björnnson, A., K. Saemundsson, P. Einarsson, E. Tryggvason, and K. Grönvold (1977), Current rifting episode in north Iceland, *Nature*, *266*, 318–323.

Bohrson, W. A., and F. J. Spera (2001), Energy-constrained open-system magmatic processes II: application of energy-constrained assimilation-fractional crystallisation (EC-AFC) model to magmatic systems, *J. Petrol.*, *42*(5), 1019–1041.

Braun, J., and C. Beaumont (1989), A physical explanation of the relation between flank uplifts and the breakup unconformity at rifted continental margins, *Geology*, *17*, 760–764.

Brown, M. (2007), Crustal melting and melt extraction, ascent and emplacement in orogens: Mechanisms and consequences, *J. Geol. Soc.*, *164*, 709–730.

Brown, M. (2010a), Melting of the continental crust during orogenesis: The thermal, rheological, and compositional consequences of melt transport from lower to upper continental crust, *Can. J. Earth Sci.*, *47*, 655–694.

Brown, M. (2010b), The spatial and temporal patterning of the deep crust and implications for the process of melt extraction, *Philos. Trans. R. Soc. London, Ser. A*, *368*, 11–51.
Brown, M. (2013), Granite: From genesis to emplacement, *Geol. Soc. Am. Bull.*, *125*, 1079–1113.
Buck, W. R. (1991), Modes of continental lithospheric extension, *J. Geophys. Res.*, *96*, 20,161–20,178, doi:10.1029/91JB01485.
Buck, W. R. (2004), Consequences of asthenospheric variability on continental rifting, in *Rheology and Deformation of the Lithosphere at Continental Margins*, edited by G. D. Karner et al., pp. 1–31, Columbia Univ. Press, Palisades, N. Y.
Buck, W. R. (2006), The role of magma in the development of the Afro-Arabian Rift System, in *The Afar Volcanic Province within the East African Rift System*, edited by G. Yirgu, C. J. Ebinger, and P. K. H. Maguire, *Geol. Soc. London, Spec. Publ.*, *259*, 43–54.
Bunger, A. P., T. Menand, A. Cruden, X. Zhang, and H. Halls (2013), Analytical predictions for a natural spacing within dyke swarms, *Earth Planet. Sci. Lett.*, *375*, 270–279.
Burov, E., and S. Cloetingh (2009), Controls of mantle plumes and lithospheric folding on modes of intraplate continental tectonics: Differences and similarities, *Geophys. J. Int.*, *178*, 1691–1722.
Burov, E., and T. Gerya (2014), Asymmetric three-dimensional topography over mantle plumes, *Nature*, *513*, 85–89.
Burov, E., L. Guillou-Frottier, E. d'Acremont, L. Le Pourhiet, and S. Cloetingh (2007), Plume head–lithosphere interactions near intra-continental plate boundaries, *Tectonophysics*, *434*, 15–38, doi:10.1016/j.tecto.2007.01.002.
Caggianelli, A., and G. Prosser (2001), An exposed cross-section of late Hercynian upper and intermediate continental crust in the Sila nappe (Calabria, southern Italy), *Period. Min.*, *70*(3), 277–301.
Caggianelli, A., and G. Prosser (2002), Modelling the thermal perturbation of the continental crust after intraplating of thick granitoid sheets: A comparison with the crustal sections in Calabria (Italy), *Geolog. Mag.*, *139*(6), 699–706.
Carmichael, R. S. (1990), *Practical Handbook of Physical Properties of Rocks and Minerals*, 741 pp., CRC-Press, Boca Raton, Fla.
Cashman, K. V., and L. M. Ferry (1988), Crystal size distribution (CSD) in rocks and the kinetics and dynamics of crystallization—III. Metamorphic crystallization, *Contrib. Mineral. Petrol.*, *99*, 401–415.
Christensen, J. N., J. L. Rosenfeld, and D. J. Depaolo (1989), Rates of tectonometamorphic processes from rubidium and strontium isotopes in garnet, *Science*, *244*(4911), 1465–1469.
Christensen, J. N., J. Selverstone, J. L. Rosenfeld, and D. J. DePaolo (1994), Correlation by Rb-Sr geochronology of garnet growth histories from different structural levels within the Tauern Window, Eastern Alps, *Contrib. Mineral. Petrol.*, *18*, l–12.
Clauser, C. (2009), Heat transport processes in the Earth's crust, *Surv. Geophys.*, *30*, 163–191.
Clauser, C., and E. Huenges (1995), Thermal conductivity of rocks and minerals, in *Rock Physics and Phase Relations: A Handbook of Physical Constants, AGU Ref. Shelf 3*, edited by T. J. Ahrens, pp. 105–126, AGU, Washington, D. C.
Cloetingh, S., J. Gallart, G. de Vicente, and L. Matenco (2011), TOPO-EUROPE: From Iberia to the Carpathians and analogues, *Tectonophysics*, *502*, 1–27.
Cloetingh, S., E. Burov, L. Matenco, F. Beekman, F. Roure, and P. A. Ziegler (2013a), The Moho in extensional tectonic settings: Insights from thermo-mechanical models, *Tectonophysics*, *609*, 558–604.
Cloetingh, S., E. Burov, and T. Francois (2013b), Thermo-mechanical controls on intra-plate deformation and the role of plume-folding interactions in continental topography, *Gondwana Res.*, doi:10.1016/j.gr.2012.11.012.
Daniels, K. A., I. D. Bastow, D. Keir, R. S. J. Sparks, and T. Menand (2014), Thermal models of dyke intrusion during development of continent-ocean transition, *Earth Planet. Sci. Lett.*, *385*, 145–153.
Del Moro, A., A. Fornelli, and G. Piccarreta (2000), Tectonothermal history of the Hercynian continental crust of the Serre (southern Calabria, Italy) monitored by Rb/Sr biotite resetting, *Terra Nova*, *12*, 239–244.
Dingwell, D. B. (1995), Viscosity and anelasticity of melts, in *Mineral Physics and Crystallography: A Handbook of Physical Constants, AGU Ref. Shelf 2*, edited by T. J. Ahrens, pp. 209–217, AGU, Washington, D. C.
Dunbar, J. A., and D. S. Sawyer (1989), How pre-existing weaknesses control the style of continental breakup, *J. Geophys. Res.*, *94*, 7278–7292, doi:10.1029/JB094iB06p07278.
Ebinger, C. J., J. A. Jackson, A. N. Foster, N. J. Hayward, D. McKenzie, N. Kusznir, K. E. Louden, A. B. Watts, M. Menzies, and A. Roberts (1999), Extensional basin geometry and the elastic lithosphere, *Philos. Trans. R. Soc. London, Ser. A*, *357*, 741–765.
Gaidies, F., D. R. M. Pattison, and C. de Capitani (2011), Toward a quantitative model of metamorphic nucleation and growth, *Contrib. Mineral. Petrol.*, *162*, 975–993.
Gerya, T. (2010), *Introduction to Numerical Geodynamic Modelling*, 345 pp., Cambridge Univ. Press, U. K.
Gleason, G. C., and J. Tullis (1995), A flow law for dislocation creep of quartz aggregates determined with the molten salt cell, *Tectonophysics*, *247*, 1–23.
Hayward, N. J., and C. Ebinger (1996), Variations in the along-axis segmentation of the Afar Rift system, *Tectonophysics*, *15*, 244–257.
Hjartardóttir, A. R., P. Einarsson, E. Bramham, and T. J. Wright (2012), The Krafla fissure swarm, Iceland, and its formation by rifting events, *Bull. Volcanol.*, *74*, 2139–2153, doi:10.1007/s00445-012-0659-0.
Holbrook, W. S., G. M. Purdy, J. A. Collins, R. E. Sheridan, D. L. Musser, L. Glover, M. Talwani, J. I. Ewing, R. Hawman, and S. B. Smithson (1992), Deep velocity structure of rifted continental crust, U.S. Mid-Atlantic Margin, from wide-angle reflection/refraction data, *Geophys. Res. Lett.*, *19*, 1699–1702, doi:10.1029/92GL01799.
Holland, T. J. B., and R. Powell (1998), An internally consistent thermodynamic data set for phases of petrological interest, *J. Metamorph. Geol.*, *16*, 309–343.
Holness, M. B., and E. W. Sawyer (2008), On the pseudomorphing of melt-filled pores during the crystallization of migmatites, *J. Petrol.*, *49*, 1343–1363.
Huismans, R. S., S. J. H. Buiter, and C. Beaumont (2005), Effect of plastic-viscous layering and strain softening on mode selection during lithospheric extension, *J. Geophys. Res.*, *110*, B02406, doi:10.1029/2004JB003114.
Incropera, F. P., D. P. DeWitt, T. L. Bergman, and A. S. Lavine (2006), *Fundamentals of Heat and Mass Transfers*, 997 pp., Wiley, Hoboken, N. J.
Jessop, A. M., and L. Trevor (1978), Heat flow and heat generation in the superior province of the Canadian shield, *Tectonophysics*, *50*(1), 55–77.
Ji, S., and P. Zhao (1993), Flow laws of multiphase rocks calculated from experimental data on the constituent phases, *Earth Planet. Sci. Lett.*, *117*, 181–187.
Ji, S., P. Zhao, and X. Bia (2003), Flow laws of multiphase materials and rocks from end-member flow laws, *Tectonophysics*, *370*, 129–145.
Karato, S. I. (2008), *Deformation of Earth Materials*, 463 pp., Cambridge Univ. Press, U. K.
Keir, D., C. J. Ebinger, G. W. Stuart, E. Daly, and A. Ayele (2006), Strain accommodation by magmatism and faulting as rifting proceeds to breakup: Seismicity of the northern Ethiopian rift, *J. Geophys. Res.*, *111*, B05314, doi:10.1029/2005JB003748.
Kirby, S. H. (1985), Rock mechanics observations pertinent to the rheology of the continental lithosphere and the localization of strain along the shear zones, *Tectonophysics*, *119*, 1–27.

Kronenberg, A. K., S. H. Kirby, and J. Pinkston (1990), Basal slip and mechanical anisotropy of biotite, *J. Geophys. Res.*, *95*, 19,257–19,278, doi:10.1029/JB095iB12p19257.
Kruhl, J. H., and R. H. Vernon (2005), Syndeformational emplacement of a tonalitic sheet-complex in a late-Variscan thrust regime: Fabrics and mechanism of intrusion, Monte'E Senes, Northeastern Sardinia, Italy, *Can. Mineral.*, *43*, 387–407.
Kruhl, J. H., S. Erdmann, and S. H. Büttner (2007), Brittle-ductile microfabrics in naturally deformed cordierite: Evidence for significant short-term strain-rate variations, *J. Struct. Geol.*, *29*, 355–374.
Lachenbruch, A. H. (1968), Preliminary geothermal model of the Sierra Nevada, *J. Geophys. Res.*, *73*, 6977–6990, doi:10.1029/JB073i022p06977.
Laporte, D., and E. B. Watson (1995), Experimental and theoretical constraints on melt distribution in crustal sources: The effect of crystalline anisotropy on melt interconnectivity, *Chem. Geol.*, *124*, 161–184.
Logg, A., K. A. Mardal, and G. Wells (Eds.) (2012), *Automated Solution of Differential Equations by the Finite Element Method*, 723 pp., Springer, London.
Laube, N., and J. Springer (1998), Crustal melting by ponding of mafic magmas: A numerical model, *J. Volcanol. Geotherm. Res.*, *81*, 19–35.
Luth, W. C., R. I. Jahns, and O. F. Tuttle (1964), The granite system at pressures of 4 to 10 kilobars, *J. Geophys. Res.*, *69*, 759–773, doi:10.1029/JZ069i004p00759.
Maccaferri, F., E. Rivalta, D. Keir, and V. Acocella (2014), Off-rift volcanismin rift zones determined by crustal unloading, *Nat. Geosci.*, *7*, 297–300, doi:10.1038/NGEO2110.
Marchildon, N., and M. Brown (2002), Grain-scale melt distribution in two contact aureole rocks: Implications for controls on melt localization and deformation, *J. Metamorph. Geol.*, *20*, 381–396.
McKenzie, D. P. (1978), Some remarks on the development of sedimentary basins, *Earth Planet. Sci. Lett.*, *40*, 25–32.
Michaut, C., and C. Jaupart (2006), Ultra-rapid formation of large volumes of evolved magma, *Earth Planet. Sci. Lett.*, *250*, 38–52, doi:10.1016/j.epsl.2006.07.019.
Mohr, P. (1991), Nature of the crust beneath magmatically active continental rifts, *Tectonophysics*, *213*, 269–284.
Natali, C., L. Beccaluva, G. Bianchini, and F. Siena (2011), Rhyolites associated to Ethiopian CFB: Clues for initial rifting at the Afar plume axis, *Earth Planet. Sci. Lett.*, *312*, 59–68.
Natarov, S. I., and C. P. Conrad (2012), The role of Poiseuille flow in creating depth-variation of asthenospheric shear, *Geophys. J. Int.*, *190*, 1297–1310.
Paterson, S. R., T. K. Fowler Jr., K. L. Schmidt, A. S. Yoshinobu, E. S. Yuan, and R. B. Miller (1998), Interpreting magmatic fabric patterns in plutons, *Lithos*, *44*, 53–82.
Patiño Douce, A. E., and A. D. Johnston (1991), Phase equilibria and melt productivity in the pelitic system: Implications for the origin of peraluminous granitoids and aluminous granulites, *Contrib. Mineral. Petrol.*, *107*, 202–218.
Pattison, D. R. M., and D. L. Tinkham (2009), Interplay between equilibrium and kinetics in metamorphism of pelites in the Nelson aureole, British Columbia, *J. Metamorph. Geol.*, *27*, 249–279.
Philpotts, A. R., and J. J. Ague (2009), *Principles of Igneous and Metamorphic Petrology*, 667 pp., Cambridge Univ. Press, Cambridge, U. K.
Ranalli, G. (1995), *Rheology of the Earth*, 414 pp., Chapman and Hall, London, U. K.
Roscoe, R. (1952), The viscosity of suspensions of rigid spheres, *Brit. J. Appl. Phys.*, *3*, 267–269.
Rosenberg, C. L., and M. R. Handy (2005), Experimental deformation of partially melted granite revisited: Implications for the continental crust, *J. Metamorph. Geol.*, *23*, 19–28.
Rudnick, R. L., and S. Gao (2003), Composition of the continental crust, in *Treatise on Geochemistry*, vol. III, edited by H. D. Holland and K. K. Turekian, pp. 1–64, Elsevier.
Rychert, C. A., J. O. S. Hammond, N. Harmon, J. M. Kendall, D. Keir, C. Ebinger, I. D. Bastow, A. Ayele, M. Belachew, and G. Stuart (2012), Volcanism in the Afar Rift sustained by decompression melting with minimal plume influence, *Nat. Geosci.*, *5*, 406–409.
Sawyer, E. W. (2001), Melt segregation in the continental crust: Distribution and movement of melt in anatectic rocks, *J. Metamorph. Geol.*, *19*, 291–309.
Shaw, H. R. (1965), Comments on viscosity, crystal settling, and convection in granitic magmas, *Am. J. Sci.*, *263*, 120–152.
Shelton, G., and J. Tullis (1981), *Experimental Flow Laws for Crustal Rocks, Eos Trans*, vol. 62, 396 pp., AGU, Washington, D. C.
Sibson, R. H. (1974), Frictional constraints on thrust, wrench and normal faults, *Nature*, *249*, 542–544.
Solano, J. M. S., M. D. Jackson, R. S. J. Sparks, J. D. Blundy, and C. Annen (2012), Melt segregation in deep crustal hot zones: A mechanism for chemical differentiation, crustal assimilation and the formation of evolved magmas, *J. Petrol.*, *53*, 1999–2026, doi:10.1093/petrology/egs041.
Sonder, L. J. P. C. E., B. P. Wernicke, and R. L. Christiansen (1987), *A Physical Model for Cenozoic Extension of Western North America*, *Geol. Soc. London, Spec. Publ.*, *28*, 187–201.
Spear, F. S. (1993), *Metamorphic Phase Equilibria and Pressure-Temperature-Time Paths Mineral*, 799 pp., Mineral. Soc. Am., Washington, D. C.
Spear, F. S., and J. T. Cheney (1989), A petrogenetic grid for pelitic schists in the system SiO_2-Al_2O_3-FeO-MgO-K_2O-H_2O, *Contrib. Mineral. Petrol.*, *101*, 149–164.
Symmes, G. H., and J. M. Ferry (1992), The effect of whole-rock MnO content on the stability of garnet in pelitic schists during metamorphism, *J. Metamorph. Geol.*, *10*, 221–237.
Vielzeuf, D., and J. R. Holloway (1988), Experimental determination of the fluid-absent melting relations in the pelitic system. Consequences for crustal differentiation, *Contrib. Mineral. Petrol.*, *98*, 257–276.
Vilà, M., M. Fernàndez, and I. Jimènez-Munt (2010), Radiogenic heat production variability of some common lithological groups and its significance to lithospheric thermal modelling, *Tectonophysics*, *490*, 152–164.
Wang, Z., and S. Ji (1999), Deformation of silicate garnets: Brittle-ductile transition and its geological implications, *Can. Mineral.*, *37*, 525–541.
Wilson, L. (1981), Ascent and Eruption of Basaltic Magma on the Earth and Moon, *J. Geophys. Res.*, *86*, 2971–3001, doi:10.1029/JB086iB04p02971.
Wolfenden, E., C. Ebinger, G. Yirgu, A. Deino, and D. Ayalew (2004), Evolution of the northern Main Ethiopian rift: Birth of a triple junction, *Earth Planet. Sci. Lett.*, *224*, 213–228.
Wright, T. J., C. Ebinger, J. Biggs, A. Ayele, G. Yirgu, D. Keir, and A. Stork (2006), Magma-maintained rift segmentation at continental rupture in the 2005 Afar dyking episode, *Nature*, *42*, 291–294.
Wright, T. J., et al. (2012), Geophysical constraints on the dynamics of spreading centres from rifting episodes on land, *Nat. Geosci.*, *5*, 242–250, doi:10.1038/NGEO1428.
Ziegler, P. A., and S. Cloetingh (2004), Dynamic processes controlling the evolution of rifted basins, *Earth Sci. Rev.*, *64*, 1–50.
Zoth, G., and R. Hänel (1988), Appendix, in *Handbook of Terrestrial Heat Flow Density Determination*, edited by R. Hänel, L. Rybach, and L. Stegena, pp. 449–466, Kluwer, Dordrecht.